

Fine-Tuning Alkyl Chains on Quinoxaline Nonfullerene Acceptors Enables High-Efficiency Ternary Organic Solar Cells with Optimizing Molecular Stacking and Reducing Energy Loss

Yuntong Guo, Zhenyu Chen, Jinfeng Ge, Jintao Zhu, Jinna Zhang, Yuanyuan Meng, Qinrui Ye, Shijie Wang, Fei Chen, Wei Ma,* and Ziyi Ge*

Material design of guest acceptor is always a big challenge for improving the efficiency of ternary organic solar cells (OSCs). Here, a pair of isomeric nonfullerene acceptors based on quinoxaline core, Qx-*p*-C₇H₈O and Qx-*m*-C₇H₈O, is designed and synthesized. By moving the alkoxy chain attached on side phenyl from *meta*-position to *para*-position, both π - π stacking distance and crystallinity are enhanced simultaneously. They obtain the uplifted lowest unoccupied molecular orbital level. Compared to Qx-*m*-C₇H₈O, Qx-*p*-C₇H₈O exhibits wider absorption spectrum and higher extinction coefficient. Using D18-Cl:N3 as host materials, the addition of guest acceptor Qx-*p*-C₇H₈O significantly improves the power conversion efficiency (PCE) from 17.61% to 18.49% because of higher open-circuit voltage (0.875 V) and short-circuit current density (27.85 mA cm⁻²). This can be attributed to the faster exciton dissociation, more balanced carrier mobility, fine fiber morphology, and lower energy loss in the ternary devices. However, Qx-*m*-C₇H₈O-based ternary device achieves relatively low PCE of 17.17% because this device shows extremely low electron mobility. The results indicate that molecular stacking, film morphology, etc., can be effectively modulated by fine-tuning the side chains of guest materials, which may be an effective design rule for further improving the PCE of OSCs.

1. Introduction

Organic solar cells (OSCs) have many benefits such as solution processability, low cost, mechanical flexibility, and semitransparency, which attract significant

interest in both academic and industrial fields.^[1–3] Power conversion efficiency (PCE) of OSCs has been continuously developed. Nonfullerene acceptors (NFAs), which have received much attention in recent years, have promoted the PCE of single-junction OSCs to realize over 19% in recent years.^[4] The capacities of light absorption, exciton dissociation, charge transfer, and aggregation morphology are the primary factors of excellent OSC performance.^[5] More strategies must be used to enhance all or some of the abovementioned capabilities and thereby increase OSC performance.

Ternary strategy is one of the most effective methods to improve the performance of OSCs.^[5–9] The key challenges of ternary strategy are selecting appropriate guest component.^[10,11] The ternary strategy seeks to maximize photon collection and optimize energy level alignment and morphology. When guest component with comparable absorption spectra and a higher extinction coefficient is incorporated, ternary

device can capture more photons from the solar spectrum and obtain higher short-circuit current density (I_{SC}).^[4,12] To create efficient charge-transport channels and improve V_{OC} in ternary devices, it is essential for the guest component to have the suitable highest occupied molecular orbital (HOMO) and lowest

Y. Guo, Z. Chen, J. Ge, J. Zhang, Y. Meng, Q. Ye, Z. Ge
 Ningbo Institute of Materials Technology and Engineering
 Chinese Academy of Sciences
 Ningbo 315201, China
 E-mail: geziyi@nimte.ac.cn

Y. Guo
 School of Chemical Engineering
 Zhejiang University of Technology
 Hangzhou 310014, China

J. Zhu, F. Chen
 Department of Chemical and Environmental Engineering
 University of Nottingham Ningbo China
 Ningbo 315100, China

S. Wang, W. Ma
 State Key Laboratory for Mechanical Behavior of Materials
 Xi'an Jiaotong University
 Xian 710049, China
 E-mail: msewma@mail.xjtu.edu.cn

Z. Ge
 Zhejiang Engineering Research Center for Energy Optoelectronic Materials and Devices
 Ningbo 315201, China

 The ORCID identification number(s) for the author(s) of this article can be found under <https://doi.org/10.1002/adfm.202305611>

DOI: 10.1002/adfm.202305611

unoccupied molecular orbital (LUMO).^[13,14] Ternary strategy can effectively regulate phase separation. Favorable morphology can obtain excellent charge extraction and mobility, thus device can obtain high J_{SC} and filling factor (FF).

Due to the weak electron absorption capacity of the quinoxaline (Qx) group, the molecule has a higher LUMO level, and thus the OSCs exhibit a higher V_{OC} . The acceptors based on Qx core has a larger number of modification sites. The quinoid resonance effect of Qx group can decrease the recombination energy, reduce the free σ -bonds in the target molecule acceptors, and improve charge carrier transport and intermolecular packing. In recent years, most of the studies on NFAs have focused on benzotriazole core, while few studies have been reported on the Qx-based acceptors. Zhu and co-workers demonstrated that the methyl groups on quinoxaline core can influence $\pi-\pi$ interaction, affecting electron and hole mobilities. The acceptor AQx-2 without methyl groups on quinoxaline core obtained a higher PCE of 16.64% with poly[(2,6-(4,8-bis(5-(2-ethylhexyl-2-fluoro)thiophen-2-yl)-benzo)[1,2-b:4,5-b']dithiophene)-alt-(5,5-(1',3'-di-2-thienyl-5,7'-bis(2-ethylhexyl)benzo[1',2'-c:4',5'-c']dithiophene-4,8-dione) (PBDB-TF)].^[15] Later, Ge and co-workers introduced a fluorine atom and a thiophene ring on quinoxaline core, synthesized the acceptor Qx-THF. PM6:Qx-THF-based device obtained the high PCE of 17.45%.^[16] The positions of side chain can significantly influence the molecular aggregation, thereby affecting their physicochemical properties and electron mobilities of OSCs.^[17,18] Previous studies mainly focused on changing the alkyl chain length and branching sites, but few studies on substitution sites of alkyl chain, and there was less study on applying it to the NFAs with quinoxaline core. Our study can fill the gap in the application of side-chain engineering in quinoxaline core. D18-Cl is a new conjugated polymer donor material, and N3 is a derivative of Y6. N3 exhibits good solubility, electronic properties, and morphological properties due to its additional branched alkyl group. OSCs based on D18-Cl:N3 have made some progress in improving photovoltaic performance, but there is relatively little research on organic solar cells based on this system. We synthesize acceptors as guest to prepare high performance ternary OSCs.

In this work, Qx-*p*-C₇H₈O and Qx-*m*-C₇H₈O have been designed and synthesized. We used the Y-type NFAs as the molecular backbone and the Qx-fused core replaces the benzothiadiazole-fused core. The position of methoxy group is the only distinction between these two NFAs. Qx-*p*-C₇H₈O possesses *p*-methoxyphenyl, and Qx-*m*-C₇H₈O has *m*-methoxyphenyl. Compared to N3, Qx-*p*-C₇H₈O and Qx-*m*-C₇H₈O show upshifted LUMO energy level and wider bandgap. Since the center side chain of Qx-*p*-C₇H₈O has a smaller dihedral angle with the main chain than Qx-*m*-C₇H₈O, the molecular packing of Qx-*p*-C₇H₈O is more organized. Qx-*p*-C₇H₈O obtains the wider absorption spectrum and greater extinction coefficient than Qx-*m*-C₇H₈O. Qx-*p*-C₇H₈O-based ternary device obtains a much higher PCE (18.49%) than other devices, when 20 wt% Qx-*p*-C₇H₈O is incorporated in D18-Cl:N3-based binary device. However, Qx-*m*-C₇H₈O-based ternary device obtains a lower PCE (17.17%). This is due to the reduced absorption peak of the Qx-*m*-C₇H₈O part. However, Qx-*p*-C₇H₈O-based ternary blend film has a wider absorption spectrum,^[19] resulting in the highest J_{SC} (27.85 mA cm⁻²). Compared to N3, Qx-*p*-C₇H₈O and

Qx-*m*-C₇H₈O possess a higher LUMO level, both ternary devices obtain the higher V_{OC} . A well-balance between J_{SC} and V_{OC} is obtained, because of the complementing absorption and adjustable energy levels. The exciton dissociation and charge collecting in the Qx-*p*-C₇H₈O-based ternary device are more effective. Compared to D18-Cl:N3 binary device, the electron and hole mobility of Qx-*p*-C₇H₈O-based ternary device is faster and more balanced. But the electron mobility of Qx-*m*-C₇H₈O-based ternary device is extremely slow. Although all the blend films exhibit a fiber structure,^[20] the Qx-*p*-C₇H₈O-based ternary blend film shows appropriate phase separation, which is better for charge mobility.^[21] And, the addition of Qx-*p*-C₇H₈O can adjust the energetic disorder and luminescence efficiency, which can effectively reduce the total energy loss of ternary device.^[21] The efficiency improvement is mostly due to the improved photon harvesting, regulative energy level, appropriate phase separation, and optimum crystallization. Hence, the results indicate that fine-tuning alkyl chain of the central unit can effectively regulate the stacking behavior of molecules and further prepare high-performance OSCs.

2. Synthesis and Characterization

The chemical structures of the N3, Qx-*p*-C₇H₈O, and Qx-*m*-C₇H₈O, as well as the polymer donor D18-Cl, are shown in Figure 1a. In Figure S1 (Supporting Information), the synthesis procedures for Qx-*p*-C₇H₈O and Qx-*m*-C₇H₈O were presented. By using ¹H nuclear magnetic resonance (NMR) and mass spectroscopy methods, the chemical structures of Qx-*p*-C₇H₈O and Qx-*m*-C₇H₈O were identified and verified (Figures S2–S11, Supporting Information). We used ¹H NMR methods to identify the intermediate product. The spectra are displayed in the Supporting Information. According to Figure S12a (Supporting Information), thermogravimetric analysis indicates that the thermodecomposed temperatures (with 5% weight loss) of Qx-*p*-C₇H₈O and Qx-*m*-C₇H₈O are higher than 320 °C, which is sufficient for the fabrication of OSCs as acceptor materials.^[22] Qx-*p*-C₇H₈O and Qx-*m*-C₇H₈O showed exothermal peaks from differential scanning calorimetry (DSC) studies at 288.8 and 273.2 °C, respectively (Figure S12b, Supporting Information). According to calculations, Qx-*p*-C₇H₈O and Qx-*m*-C₇H₈O have melting enthalpies (ΔH_m) of 29.24 and 29.06 J g⁻¹, respectively. In addition, the melting behavior of N3:Qx-*p*-C₇H₈O blends with different contents of Qx-*p*-C₇H₈O was studied by DSC measurements. As shown in Figure S12c (Supporting Information), the melting peaks of N3 and Qx-*p*-C₇H₈O occur at 269.3 and 288.8 °C, respectively, during the heating process. After mixing Qx-*p*-C₇H₈O with N3 with different mass ratios, the melting peak of N3:Qx-*p*-C₇H₈O mixture moves from 272.0 (0.9:0.1) to 272.2 °C (0.8:0.2). It is then moved to 272.3 °C (0.7:0.3), which indicates that N3 and Qx-*p*-C₇H₈O can be well mixed to form an alloy phase.^[23] The enthalpy of melting is proportional to its crystallinity, and the higher crystallinity a molecule has, the higher enthalpy of melting it has. The more crystallinity a molecule has, the more ordered it is. Therefore, the higher enthalpy of melting a molecule has, the more ordered it is. The findings showed that side-chain alterations might regulate molecular ordering. The regulation of thin film crystallization and morphology is largely due to this property, which is discussed in more detail

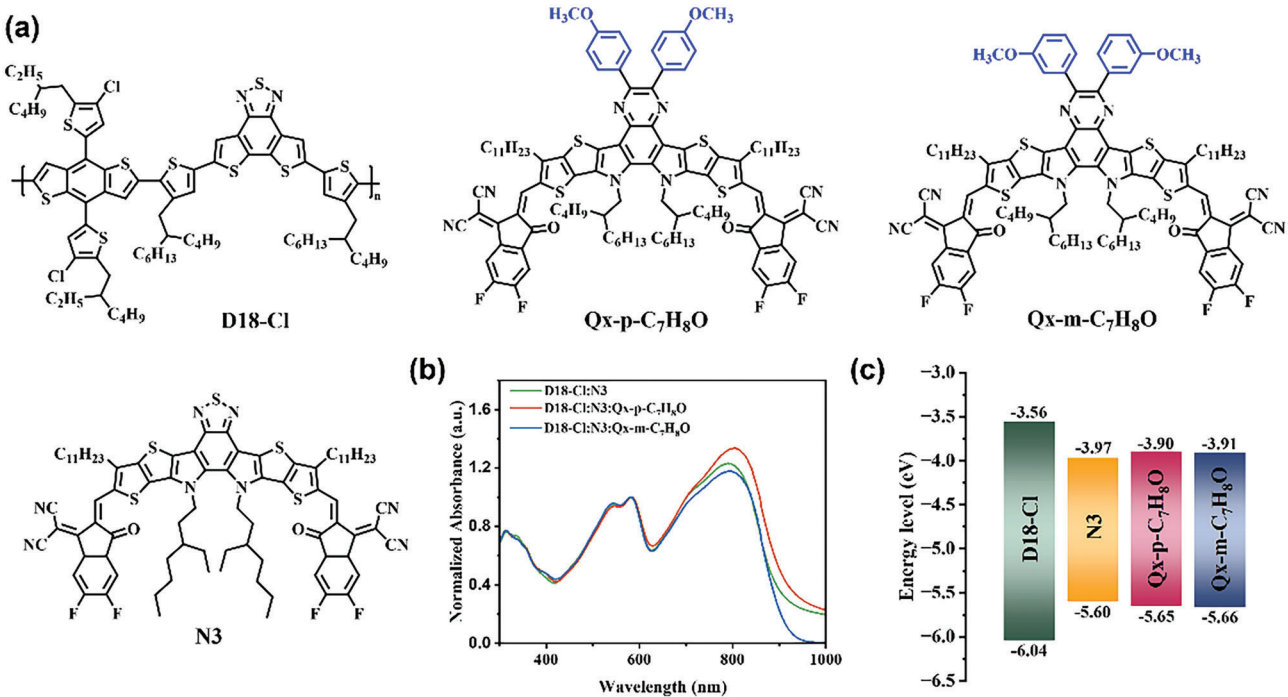


Figure 1. a) The chemical structures of the N3, Qx-p-C₇H₈O, and Qx-m-C₇H₈O, as well as the polymer donor D18-Cl; b) the UV-visible absorption spectra of the blend films; c) the energy level of donor and acceptors.

in the section on grazing incidence wide-angle X-ray scattering (GIWAXS).

We used density functional theory (DFT) computations to learn more about the molecular shape, energy level distribution, and charge distribution.^[24] At the B3LYP/6-31G(d, p) level, molecular models of the Qx-p-C₇H₈O and Qx-m-C₇H₈O acceptors were built and analyzed. The inside and outside alkyl chains were replaced by the methyl groups to make the computation easier. The optimized shapes show that Qx-p-C₇H₈O and Qx-m-C₇H₈O have comparable banana-shaped backbones. The molecule dipole moment is very different. Compared to N3, which has a dipole moment of 1.07 D, Qx-p-C₇H₈O and Qx-m-C₇H₈O acceptors have a larger dipole moment of 3.83 and 3.00 D, respectively, heading in an opposite direction.^[20] On their van der Waals surfaces, the electrostatic potential (ESP) distributions^[25,26] of N3, Qx-p-C₇H₈O, and Qx-m-C₇H₈O acceptors were plotted. The electron-deficient and electron-rich characteristics of N3, Qx-p-C₇H₈O, and Qx-m-C₇H₈O are reflected in the ESP distribution. Compared to N3, the cores of Qx-p-C₇H₈O and Qx-m-C₇H₈O show negative ESP. Figure S13 (Supporting Information), depicts the LUMO and HOMO for the two molecules. For Qx-p-C₇H₈O and Qx-m-C₇H₈O, LUMO spreads on the center and end units while HOMO only spreads on the center. It is predictable that the different alkyl chain orientations have a significant impact on molecular packing.^[27] Because of having smaller dihedral angles in its molecule geometry, Qx-p-C₇H₈O displays generally stronger intermolecular packing than Qx-m-C₇H₈O.^[17,28] The LUMO and HOMO energy levels of Qx-p-C₇H₈O and Qx-m-C₇H₈O were calculated to be -3.45/-5.46, -3.47/-5.50 eV, respectively. These findings show that the optical and electrochemical characteristics of

NFAs can be slightly tuned by varying the central conjugation degrees and alkyl chain, which is advantageous for obtaining higher J_{SC} and V_{OC} .^[29,30]

The UV-visible absorption spectra^[13] of the blend films are shown in Figure 1b and the UV-visible absorption spectra^[13] of the donor and acceptors in the film are shown in Figure S14 (Supporting Information). To facilitate comparison, all the spectra are normalized at 582 nm. Strong absorption region of D18-Cl is seen in the 400–600 nm. Furthermore, D18-Cl exhibits the highest absorption peaks at 530 nm. In the 650–900 nm region, N3, Qx-p-C₇H₈O, and Qx-m-C₇H₈O show strong absorption. Qx-p-C₇H₈O shows a redshifted absorption edge in comparison to N3 and Qx-m-C₇H₈O. The absorption peaks of Qx-p-C₇H₈O and Qx-m-C₇H₈O appear at 810 and 808 nm, while the absorption peak of N3 appears at 814 nm. While N3 and Qx-m-C₇H₈O have almost weaker normalized absorption intensity at 1000 nm than Qx-p-C₇H₈O. The absorbance edge of the thin film was used to calculate the optical bandgap, $E_g^{\text{opt}} = 1240/\lambda_{\text{onset}}$. E_g^{opt} of N3, Qx-p-C₇H₈O, and Qx-m-C₇H₈O are 1.34, 1.37, and 1.36 eV, respectively. There is a larger optical bandgap in Qx-p-C₇H₈O. N3, Qx-p-C₇H₈O, and Qx-m-C₇H₈O have shoulder peaks that can be seen in orderly films, indicating that these three NFAs have strong interactions in the solid state. Additionally, there is favorable synergistic effect in absorption between N3/Qx-p-C₇H₈O and D18-Cl. The UV-visible absorption spectrum of the blend film has the broadest range when 20 wt% Qx-p-C₇H₈O is added to D18-Cl:N3, effectively utilizing the solar spectrum. However, when Qx-m-C₇H₈O was added as the guest group, the UV-visible absorption spectrum of the blend film has the most narrow range and the absorption intensity of the acceptor region was significantly decreased. Hence,

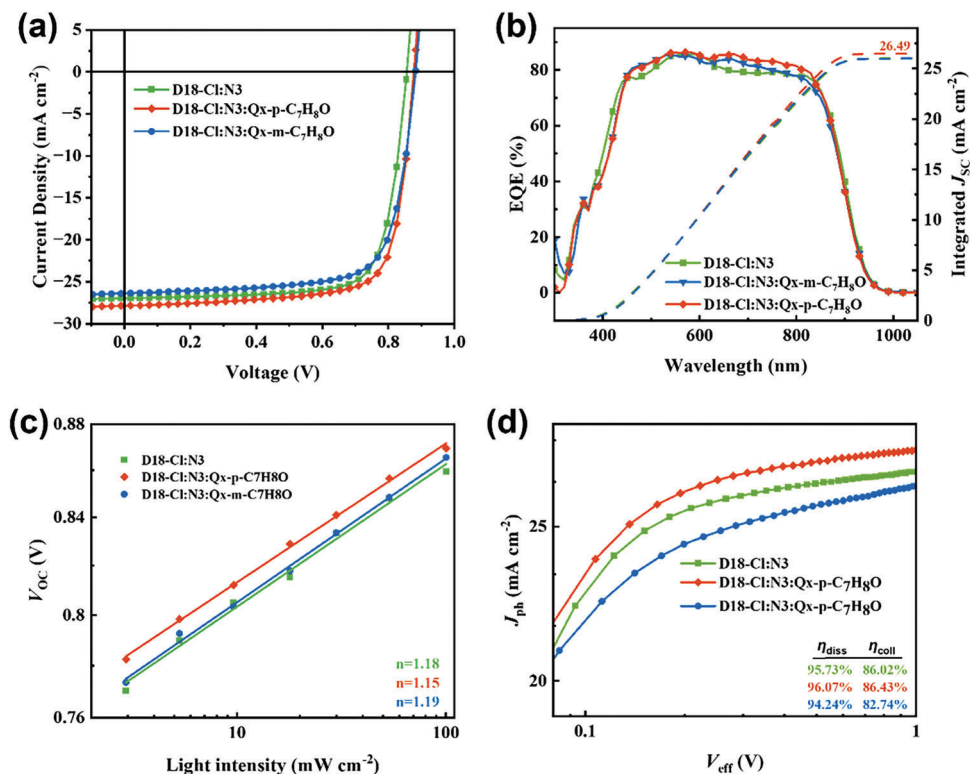


Figure 2. a) J - V curves; b) EQE curves; c) V_{OC} - $\ln P_{\text{light}}$ spectra; d) J_{ph} - V_{eff} curve of OSCs with D18-Cl:N3, D18-Cl:N3:Qx-*p*-C₇H₈O, and D18-Cl:N3:Qx-*m*-C₇H₈O.

Qx-*p*-C₇H₈O-based ternary device achieves the highest J_{SC} (27.85 mA cm⁻²), Qx-*m*-C₇H₈O-based ternary device achieves the lowest J_{SC} (26.36 mA cm⁻²).

As shown in Figure S15 (Supporting Information), the energy levels of the D18-Cl, N3, Qx-*p*-C₇H₈O, and Qx-*m*-C₇H₈O have been tested by cyclic voltammetry.^[11] In Table S1 (Supporting Information), the physical, chemical characteristics and energy levels of the donors and acceptors are listed. According to the equation $E_{\text{LUMO/HOMO}} = -(E_{\text{red/ox}} + 4.8)$ (eV), where the unit of $E_{\text{red/ox}}$ is V, the HOMO energy level (E_{HOMO}) and the LUMO energy level (E_{LUMO}) were calculated using the onset oxidation potential (E_{ox}) and onset reduction potential (E_{red}). According to estimates, the E_{LUMO} and E_{HOMO} of Qx-*p*-C₇H₈O were -3.90 and -5.65 eV, respectively, while those values for Qx-*m*-C₇H₈O were -3.91 and -5.56 eV. E_{LUMO} and E_{HOMO} of N3 were calculated to be -3.97 and -5.60 eV, respectively (Figure 1c). In both the DFT calculation and the cyclic voltammetry experiments, Qx-*p*-C₇H₈O and Qx-*m*-C₇H₈O exhibit the broader bandgap and relatively higher E_{LUMO} and lower E_{HOMO} than N3. Such result suggests that the addition of central unit conjugation degree can effectively increase the bandgap of acceptors, decrease the HOMO level, and upshift the LUMO level. The wide bandgap polymer D18-Cl was chosen as the polymer donor after taking into consideration the complementary absorption and well-matched energy levels of the donor and acceptor materials. When compared to D18-Cl:N3, Qx-*p*-C₇H₈O- and D18-Cl:N3:Qx-*m*-C₇H₈O-based ternary devices have the greater V_{OC} (0.875 and 0.880 V) due to the increased central unit conjugation degree (0.861 V).

Subsequent contact angle test indicated that N3 and two new acceptors should combine well to form composites that approximate alloys in relevant Blhk heterojunction (BHJ) blend film.^[6] Because they possess extremely similar chemical structures. We tested the contact angles of water and glycol on the donor and acceptors films, as shown in Figure S16 (Supporting Information), to further demonstrate whether N3 and two new acceptors can form alloy composites. The neat films of D18-Cl, N3, Qx-*p*-C₇H₈O, and Qx-*m*-C₇H₈O have surface tension (γ) values of 24.38, 27.33, 26.58, and 27.78 mN m⁻¹, respectively. Due to the high polarity of the terminal group connected to NFAs, N3, Qx-*p*-C₇H₈O, and Qx-*m*-C₇H₈O showed more surface tension than D18-Cl. Because the surface tensions of N3, Qx-*p*-C₇H₈O, and Qx-*m*-C₇H₈O are so close, it is likely that they will combine to create an alloy acceptor. Using the formula $\chi_{\text{D:A}} = K(\sqrt{\gamma_{\text{D}}} - \sqrt{\gamma_{\text{A}}})^2$ can calculate the surface free energy between two different materials (χ is Flory-Huggins interaction parameter, K is a constant). The result shows that $\chi(\text{N3/Qx-}p\text{-C}_7\text{H}_8\text{O}) = 0.0067\text{K}$ and $\chi(\text{N3/Qx-}p\text{-C}_7\text{H}_8\text{O}) = 0.0018\text{K}$ are obviously lower than $\chi(\text{D18-Cl:N3}) = 0.08\text{K}$, $\chi(\text{D18-Cl:Qx-}p\text{-C}_7\text{H}_8\text{O}) = 0.04\text{K}$, and $\chi(\text{D18-Cl:Qx-}m\text{-C}_7\text{H}_8\text{O}) = 0.11\text{K}$. Hence, it shows that N3, Qx-*p*-C₇H₈O, and Qx-*m*-C₇H₈O have better miscibility. The smaller interaction parameters of N3 with Qx-*p*-C₇H₈O or Qx-*m*-C₇H₈O further prove that they form an alloying phase.

Both binary and ternary OSCs were fabricated using the usual device construction of indium tin oxide/poly(3,4-ethylenedioxythiophene):poly(styrenesulfonic acid)/active layer/*N,N'*-bis[3-(dimethylamino)propyl]perylene-3,4,9,10-tetracarboxylic diimide/Ag. The Supporting Information contains a full

Table 1. The associated photovoltaic parameters of three OSCs.

Active layer	V_{OC} [V]	J_{SC} [mA cm ⁻²]	J_{SC}^{cal} [mA cm ⁻²]	FF [%]	PCE [%]
D18-Cl:N3	0.861	26.89	26.00	76.04	17.61 (17.53 ± 0.28)
D18-Cl:N3:Qx-p-C ₇ H ₈ O	0.875	27.85	26.49	75.88	18.49 (18.30 ± 0.19)
D18-Cl:N3:Qx-m-C ₇ H ₈ O	0.880	26.36	25.98	73.99	17.17 (16.95 ± 0.22)

description of the detailed fabrication of OSCs. Under simulated AM 1.5 G illumination at 100 mW cm⁻², Figure 2a and Figure S17 (Supporting Information) show the current density versus voltage ($J-V$) curves of OSCs with various active layer materials, and Table 1 lists the associated photovoltaic parameters. The D18-Cl:N3-based binary OSCs achieved a J_{SC} of 26.89 mA cm⁻², a V_{OC} of 0.861 V, and a FF of 76.04%, this resulted in a PCE of 17.61%. The J_{SC} gradually improves as the Qx-p-C₇H₈O content is added up to 20%, and then it gradually deteriorates as additional Qx-p-C₇H₈O is incorporated. As anticipated, the V_{OC} exhibits gradual promotion with the increase of Qx-p-C₇H₈O content, which should be benefited by the high LUMO energy level of Qx-p-C₇H₈O and the alloy-like behavior of the two NFAs. As a result, Qx-p-C₇H₈O-based device achieves the optimal PCE of 18.49% with a J_{SC} of 27.85 mA cm⁻², and shows an improvement over the binary device. However, Qx-m-C₇H₈O-based ternary device achieves a PCE of 17.17% with a J_{SC} of 26.36 mA cm⁻², a FF of 73.99%, and a V_{OC} of 0.880 V. Moreover, Qx-m-C₇H₈O-based binary devices have the lowest J_{SC} and FF, and obtain a poor PCE of 4.63%. In Table S2 (Supporting Information), detailed characterization is implemented based on other OSCs, including the ternary OSCs with 10 wt% Qx-p-C₇H₈O, 20 wt% Qx-p-C₇H₈O, 30 wt% Qx-p-C₇H₈O, and 20 wt% Qx-m-C₇H₈O, as well as binary OSCs, in order to better investigate the effect of Qx-p-C₇H₈O content on performance enhancement.^[31]

Figure 2b and Figure S18 (Supporting Information) display the external quantum efficiency (EQE) curve of the binary and ternary devices.^[32] The EQE spectral range of the D18-Cl:N3-based devices is rather broad, ranging from 400 to 900 nm, with lower photoelectric corresponding from 600 to 850 nm. By contrast, the D18-Cl:N3:Qx-p-C₇H₈O-based OSCs exhibit comparative high EQE values in the spectral range from 600 to 850 nm. The EQE values for the D18-Cl:N3:Qx-m-C₇H₈O-based devices are quite low in the spectral range from 600 to 750 nm. It is worth noting that the EQE values of ternary OSCs are somewhat increased throughout the entire spectral range, particularly in the 600–850 nm wavelength region. The J_{SC} for Qx-p-C₇H₈O-based ternary device is 26.49 mA cm⁻², which is much higher than the J_{SC} values of D18-Cl:N3 (26.00 mA cm⁻²) and D18-Cl:N3:Qx-m-C₇H₈O devices (25.97 mA cm⁻²). Within a 5% error mismatch, all J_{SC} values match those obtained from experimental.

$J-V$ curves were obtained under different light intensities (P_{light}) to examine how the addition of Qx-p-C₇H₈O and Qx-m-C₇H₈O affected charge recombination, as shown in Figure 2c. Normal fitting of the V_{OC} and $\ln P_{light}$ using the relation $V_{OC} \propto n k \ln P_{light}$ yields a slope value.^[33] When the slope value is closer to $2kT/q$, trap-assisted recombination becomes the predominate recombination mechanism. If the slope value is significantly close to $1kT/q$, bimolecular recombination will predominate. The fitting slope values for the D18-Cl:N3-based de-

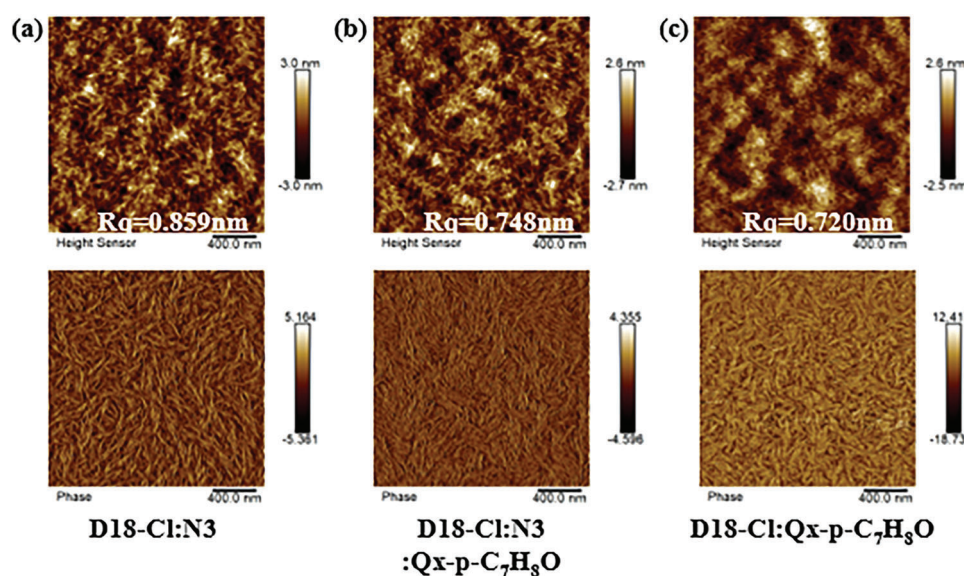
**Figure 3.** The AFM height and phase images of a) D18-Cl:N3; b) D18-Cl:N3:Qx-p-C₇H₈O; c) D18-Cl:N3:Qx-m-C₇H₈O.

Table 2. Morphological parameters obtained from GIWAXS.

Samples	In plane			Out of plane		
	Location [Å ⁻¹]	d-spacing [Å ⁻¹]	CCL [Å]	Location [Å ⁻¹]	d-spacing [Å ⁻¹]	CCL [Å]
D18-Cl:N3	0.286	22.0	63.5	1.732	3.63	23.4
D18-Cl:N3:Qx-p-C ₇ H ₈ O	0.279	22.5	78.5	1.735	3.62	26.7
D18-Cl:N3:Qx-m-C ₇ H ₈ O	0.281	22.4	63.5	1.733	3.63	24.5
Qx-p-C ₇ H ₈ O	0.262	24.0	377.0	1.744	3.60	57.1
Qx-m-C ₇ H ₈ O	0.354	17.8	33.7	1.671	3.76	17.5

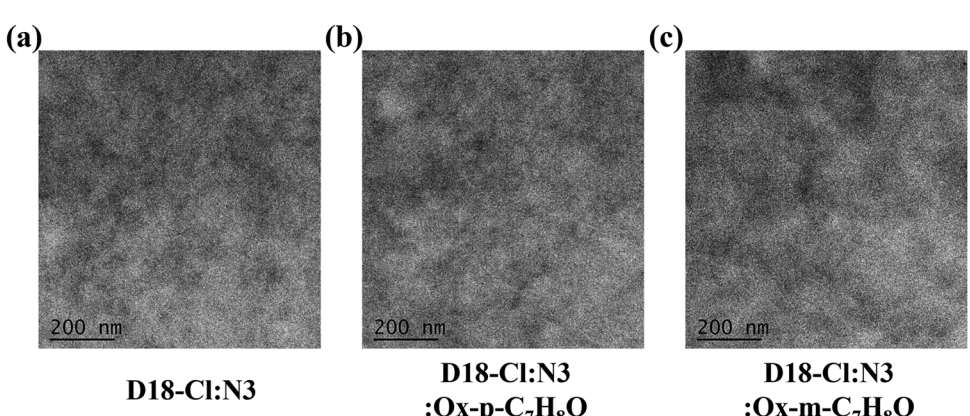
vice, D18-Cl:N3:Qx-p-C₇H₈O-based device, and D18-Cl:N3:Qx-m-C₇H₈O-based device are $1.18kT/q$, $1.15kT/q$, and $1.19kT/q$, respectively. The results show that the three devices are mainly bimolecular recombination.

The space-charge-limited current technique was used to assess the hole mobilities (μ_h) and electron mobilities (μ_e) of the binary and ternary OSCs, in order to understand the effects of adding Qx-p-C₇H₈O and Qx-m-C₇H₈O on the charge transport of the ternary OSCs.^[34] Figure S19 and Table S3 (Supporting Information) display the measurement results for the binary and ternary devices. The μ_e and μ_h values of D18-Cl:N3-based device are 9.22 and 8.04×10^{-4} cm² V⁻¹ s⁻¹, respectively. And the ratio of μ_e/μ_h is 1.15. The μ_e and μ_h values of D18-Cl:N3:Qx-p-C₇H₈O-based device were determined to be 10.81 and 9.97×10^{-4} cm² V⁻¹ s⁻¹, respectively. And the ratio of μ_e/μ_h is 1.08. Figure S19 (Supporting Information) shows that Qx-m-C₇H₈O-based ternary OSCs obtain low electron mobility with less difference in hole mobility. For Qx-m-C₇H₈O, where the larger dihedral angle of the side chain pushes neighboring molecules away, impeding the necessary p-p stacking, Qx-p-C₇H₈O exhibits stronger intermolecular stacking than Qx-m-C₇H₈O. However, it is noted that Qx-m-C₇H₈O-based device obtains considerably lower electron mobility and therefore produces the worst J_{SC} . The Qx-p-C₇H₈O-based OSC has a high and balanced charge transport, which can prevent the accumulation and recombination of charges, which is conducive to charge transport, so that the corresponding device has a high J_{SC} value.

We measured the photocurrent density (J_{ph}) versus the effective voltage (V_{eff}) to analyze the effect of the Qx-p-C₇H₈O component on the charge generation, collection, and recombination behaviors in ternary devices.^[35] The J_{ph} - V_{eff} curves of OSCs are shown in Figure 2d. J_{light} and J_{dark} represent the current densities under light and in the dark, respectively, and are used to define the J_{ph} . V_{eff} is calculated by the equation $V_{eff} = V_0 - V$, where V is the applied voltage and V_0 is the voltage at which J_{ph} is zero. For exciton dissociation, a higher V_{eff} can offer a larger interior electric field. Therefore, in order to analyze the exciton dissociation (η_{diss}) and charge collection efficiency (η_{coll}) of the OSCs, we used the values of J_{ph}^1/J_{sat} and J_{ph}^2/J_{sat} . J_{ph}^1 and J_{ph}^2 are current density of short circuit and maximal power output, and J_{sat} is saturation current density when V is 3 V. The η_{diss} and η_{coll} values of D18-Cl:N3:Qx-p-C₇H₈O are 96.07% and 86.43%, respectively. The η_{diss} and η_{coll} values of D18-Cl:N3:Qx-m-C₇H₈O are 94.24% and 82.74%, respectively. This result shows a superior exciton dissociation and charge collection in Qx-p-C₇H₈O-based ternary device. Obviously, the addition of Qx-m-C₇H₈O to D18-Cl:N3-based binary device decreases exciton dissociation probabilities and charge gathering probabilities. Effectively increased charge generation and collection and inhibited charge recombination, Qx-p-C₇H₈O was added to D18-Cl:N3-based binary device.

Additionally, Qx-p-C₇H₈O-based ternary film displayed the best photoluminescence quench efficiency of all the blend films (Figure S20, Supporting Information). This finding clearly shows that Qx-p-C₇H₈O-based ternary film is superior to other systems in terms of charge transfer and exciton dissociation efficiency, which indicates that Qx-p-C₇H₈O-based ternary OSCs not only reduce recombination but also enhance the corresponding photovoltaic properties.

To study the phase separation morphologies of the blend films, we used atomic force microscopy (AFM) and transmission electron microscopy (TEM). The three blend films based on D18-Cl:N3, D18-Cl:N3:Qx-p-C₇H₈O, and D18-Cl:N3:Qx-m-C₇H₈O exhibit extremely smooth surfaces with root mean square roughness values under 1 nm, as revealed in the AFM pictures^[36] (Figure 3). The average root-mean-square (RMS) roughnesses have decreased from 0.859 nm of D18-Cl:N3 blend film to 0.748 nm of ternary blend film with 20 wt% Qx-p-C₇H₈O. By comparing the roughness of different blend films, we found that

**Figure 4.** The TEM images of a) D18-Cl:N3 blend film; b) Qx-p-C₇H₈O-based ternary blend film; c) Qx-m-C₇H₈O-based ternary blend film.

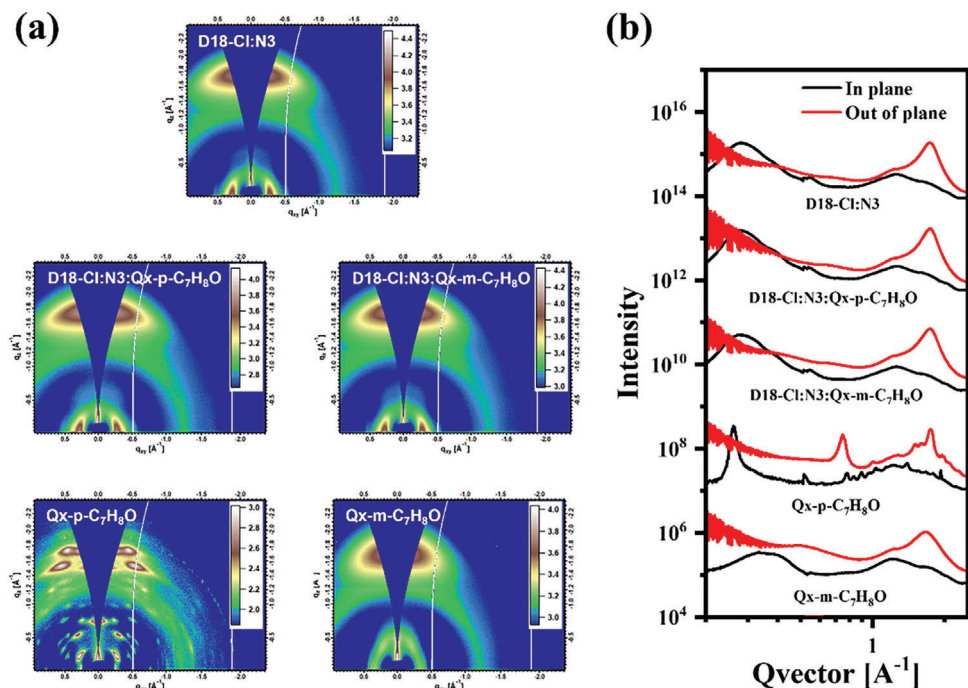


Figure 5. a) 2D GIWAXS pattern images; b) 1D line-cut profiles along the IP and OOP directions.

Qx-*p*-C₇H₈O may be utilized as a regulator to alter the phase morphology of blend films.^[4] Both the Qx-*p*-C₇H₈O ternary blend film and the binary film show clear fiber structure, and the Qx-*p*-C₇H₈O ternary film obtains smaller RMS. However, when Qx-*m*-C₇H₈O was added, although the roughness also decreased, the fiber structure in the phase diagram became fuzzy.

As shown by TEM investigation (Figure 4) the D18-Cl:N3 blend film is roughly defined with more sparse fibril distribution, which is harmful to exciton dissociation and charge transport. The boundary of Qx-*p*-C₇H₈O-based ternary blend film is clearer, and the dark and bright regions combine to form a continuous interpenetrating network structure. The charge production and extraction are positively impacted by the continuous interpenetrating networks and favorable nanoscale phase separation, which helps to significantly increase J_{SC} in the optimized OSCs. However, the TEM diagram of Qx-*m*-C₇H₈O-based blend film shows the larger molecular cluster, which explains the weak PCE of Qx-*m*-C₇H₈O-based ternary OSCs.

GIWAXS studies of the blend films were performed to learn more about the features of BHJ morphology. Figure 5a displays the GIWAXS pattern images, and Figure 5b displays the 1D line-cut profiles along the in plane (IP) and out of plane (OOP) lines. All of the thin film samples display a face-on molecular alignment, as seen in Figure S21 (Supporting Information). The Qx-*m*-C₇H₈O exhibits clear lamellar (100) diffraction peaks in the IP direction and a strong $\pi-\pi$ (010) peak in the OOP direction, suggesting a favorable face-on orientation. It is worth noting that the Qx-*p*-C₇H₈O film exhibits distinct (100), (200), and (300) diffraction peaks in the IP direction, suggesting a most ordered molecular stacking. The larger crystal coherence length (CCL) of D18-Cl:N3:Qx-*p*-C₇H₈O blend film indicates more ordered molecular packings, which should reduce energy disorder, the specific data will be covered in Table 2. For D18-Cl:N3, D18-Cl:N3:Qx-*p*-C₇H₈O, and D18-Cl:N3:Qx-*m*-C₇H₈O, the strong (010) diffraction peaks in the OOP direction at 1.732, 1.735, and 1.733 \AA^{-1} , respectively, correlative *d*-spacings are 3.63, 3.62, and 3.63 \AA^{-1} .

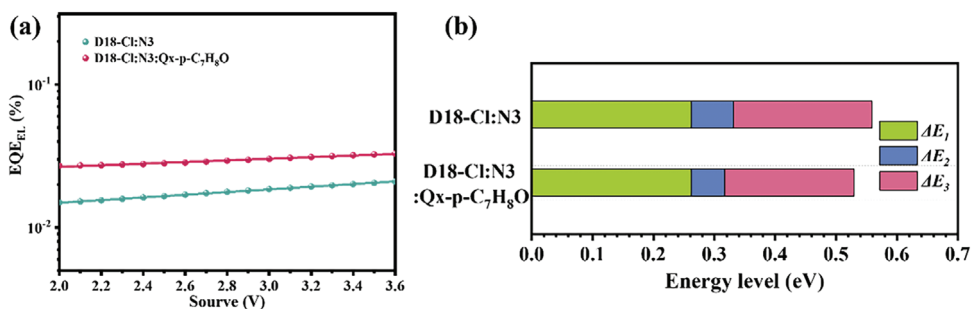


Figure 6. a) EQE_{EL} curve of binary and ternary devices; b) diagram of the recombination losses, including radiative and nonradiative.

Table 3. Detailed E_{Loss} parameters of the OSCs based on D18-Cl:N3 and D18-Cl:N3:Qx-*p*-C₇H₈O.

Active layer	V_{OC} [V]	E_g [eV]	$V^{\text{SQ}}_{\text{OC}}$ ^{a)} [V]	ΔE_1 [eV]	$V^{\text{rad}}_{\text{OC}}$ ^{b)} [V]	ΔE_2 [eV]	$\text{EQE}_{\text{EL}} \times 10^{-4}$	ΔE_3 [eV]	E_{Loss} [eV]
D18-Cl:N3	0.861	1.396	1.134	0.262	1.065	0.069	1.45	0.228	0.559
D18-Cl:N3:Qx- <i>p</i> -C ₇ H ₈ O	0.875	1.396	1.134	0.262	1.079	0.055	2.72	0.212	0.529

^{a)} $V^{\text{SQ}}_{\text{OC}}$ was calculated according to the Shockley–Queisser (SQ) theory; ^{b)} $V^{\text{rad}}_{\text{OC}}$ was calculated from EL and Fourier transform photocurrent spectroscopy (FTPS) measurements.

The D18-Cl:N3:Qx-*p*-C₇H₈O blend film exhibits more ordered molecular packings in the interpenetrating networks, after the addition of Qx-*p*-C₇H₈O as the guest component. These findings proved that Qx-*p*-C₇H₈O, a molecule with high dipole moment, can strengthen molecular packing and increase intermolecular interactions. Then, we calculated the CCL of all samples (Table S4, Supporting Information). In the OOP direction, the CCLs of D18-Cl:N3 film, Qx-*p*-C₇H₈O- and Qx-*m*-C₇H₈O-based blend films are 23.4, 26.7, and 24.5 Å, respectively. These results were attributed to dipole moment and excellent crystallinity of Qx-*p*-C₇H₈O, which allowed stronger interactions to enhance molecular packing. The crystallinity of the ternary BHJ film is better than the binary films due to the highly ordered Qx-*p*-C₇H₈O.^[37] Stronger stacking features of Qx-*p*-C₇H₈O include more compact molecular packing and longer range order, which may improve phase purity and decrease bulk defects.^[18] In summary, the side-chain engineering produces an optimal morphology with an acceptable domain size, increased phase purity, ordered and compact molecular arrangement, which lead to efficient exciton dissociation and charge extraction in the N3-based binary OSCs.^[38,39]

We evaluated the highly sensitive EQE and electroluminescence (EL) quantum efficiencies (EQE_{EL}),^[33] respectively, and further investigated the factors that contributed to the enhancement of V_{OC} in ternary device.^[40] Figure 6 and Table 3 both offer a summary of the detailed E_{loss} of the D18-Cl:N3 binary device and D18-Cl:N3:Qx-*p*-C₇H₈O ternary device. The E_g of the D18-Cl:N3- and D18-Cl:N3:Qx-*p*-C₇H₈O-based devices were both 1.396 eV, according to Figure S22 (Supporting Information). The D18-Cl:N3- and D18-Cl:N3:Qx-*p*-C₇H₈O-based devices had total E_{loss} values of 0.559 and 0.529 eV, respectively (Table 3). Figure 6a indicates that unavoidable energy loss (ΔE_1) is no discernible different. The ΔE_2 refers to the radiative recombination loss below the bandgap and is attributed to non-step-function absorption. The ΔE_2 values of the D18-Cl:N3- and D18-Cl:N3:Qx-*p*-C₇H₈O-based devices were 0.069 and 0.055 eV, respectively.

The EQE_{EL} values of D18-Cl:N3- and D18-Cl:N3:Qx-*p*-C₇H₈O-based devices are 1.45×10^{-4} and 2.72×10^{-4} , respectively (Figure 6a). The ΔE_3 values of the D18-Cl:N3- and D18-Cl:N3:Qx-*p*-C₇H₈O-based OSCs were 0.228 and 0.212 eV, respectively (Figure 6b). In conclusion, D18-Cl:N3:Qx-*p*-C₇H₈O-based ternary device showed the lowest E_{loss} (0.529 eV). The greatest V_{OC} in this ternary device is associated with the shortest ΔE_2 (0.055 eV) and ΔE_3 (0.212 eV). This finding suggests that by concurrently regulating the energetic disorder and luminescence efficiency, the addition of the appropriate guest component for the fabrication of ternary OSCs efficiently decreases the E_{loss} .^[41]

In summary, the adjustment of central unit alkyl chain can regulate molecular stacking more effectively. When we moved the alkoxy chain attached on side phenyl from *meta*-position to *para*-position, molecules obtain the smaller dihedral angles. Therefore, the Qx-*p*-C₇H₈O-based ternary blend film obtains more ordered and tight molecular packing. The D18-Cl:N3:Qx-*p*-C₇H₈O ternary device obtains the most excellent PCE of 18.49%, a V_{OC} of 0.875 V, and a J_{SC} of 27.85 mA cm^{-2} . However, D18-Cl:N3:Qx-*m*-C₇H₈O ternary device obtains the lowest PCE of 17.17%. Qx-*p*-C₇H₈O-based ternary blend film obtains wider absorption spectrum than Qx-*m*-C₇H₈O-based ternary blend film. Compared to Qx-*m*-C₇H₈O, Qx-*p*-C₇H₈O-based ternary blend film exhibits a clear fiber structure and appropriate phase separation, which is better for charge mobility, faster and more balanced exciton dissociation, and charge collection rates. But Qx-*m*-C₇H₈O-based ternary device has extremely low charge mobility. Therefore, the side-chain engineering of central unit has great influence on the performance of acceptor. Fine-tuning the alkyl chain of the central unit can effectively adjust the stacking behavior of molecules, thus preparing high-performance OSCs.

3. Statistical Analysis

Average PCE values with standard deviation obtained from ten individual devices.

Supporting Information

Supporting Information is available from the Wiley Online Library or from the author.

Acknowledgements

Y.G. and Z.C. contributed equally to this work. This work was financially supported by the National Science Fund for Distinguished Young Scholars (Grant No. 21925506), the National Natural Science Foundation of China (Grant Nos. U21A20331 and 81903743), the CAS Key Project of Frontier Science Research (Grant No. QYZDB-SSW-SYS030), and the Ningbo Natural Science Foundation (Grant No. 2021J192), the Ningbo key scientific and technological project (Grant No. 2022Z117). X-ray data were acquired at beamline 7.3.3 at the Advanced Light Source, which is supported by the Director, Office of Science, Office of Basic Energy Sciences, of the U.S. Department of Energy under Contract No. DE-AC02-05CH11231. The authors thank Dr. Eric Schable and Dr. Chenhui Zhu at beamline 7.3.3 for assistance with data acquisition, the National Key Research and Development Program of China (Grant No. 2022YFE0132400), the NSFC (Grant Nos. 21875182, 52173023), the Key Scientific and Technological Innovation Team Project of Shaanxi Province (Grant No. 2020TD-002), and the 111 project 2.0 (Grant No. BP0618008).

Conflict of Interest

The authors declare no conflict of interest.

Data Availability Statement

The data that support the findings of this study are available in the Supporting Information of this article.

Keywords

molecular stacking, nonfullerene acceptors, quinoxaline, side-chain engineering, ternary strategy

Received: May 19, 2023

Revised: July 7, 2023

Published online: August 4, 2023

- [1] M. Zhou, C. Liao, Y. Duan, X. Xu, L. Yu, R. Li, Q. Peng, *Adv. Mater.* **2023**, *35*, 2208279.
- [2] X. Xu, W. Jing, H. Meng, Y. Guo, L. Yu, R. Li, Q. Peng, *Adv. Mater.* **2023**, *35*, 2208997.
- [3] J. Ge, L. Hong, H. Ma, Q. Ye, Y. Chen, L. Xie, W. Song, D. Li, Z. Chen, K. Yu, J. Zhang, Z. Wei, F. Huang, Z. Ge, *Adv. Mater.* **2022**, *34*, 2202752.
- [4] L. Zhu, M. Zhang, J. Xu, C. Li, J. Yan, G. Zhou, W. Zhong, T. Hao, J. Song, X. Xue, Z. Zhou, R. Zeng, H. Zhu, C.-C. Chen, R. C. I. MacKenzie, Y. Zou, J. Nelson, Y. Zhang, Y. Sun, F. Liu, *Nat. Mater.* **2022**, *21*, 656.
- [5] Z. Chen, W. Song, K. Yu, J. Ge, J. Zhang, L. Xie, R. Peng, Z. Ge, *Joule* **2021**, *5*, 2395.
- [6] F. Liu, L. Zhou, W. Liu, Z. Zhou, Q. Yue, W. Zheng, R. Sun, W. Liu, S. Xu, H. Fan, L. Feng, Y. Yi, W. Zhang, X. Zhu, *Adv. Mater.* **2021**, *33*, 2100830.
- [7] S. Li, L. Zhan, N. Yao, X. Xia, Z. Chen, W. Yang, C. He, L. Zuo, M. Shi, H. Zhu, X. Lu, F. Zhang, H. Chen, *Nat. Commun.* **2021**, *12*, 4627.
- [8] Y. Cui, Y. Xu, H. Yao, P. Bi, L. Hong, J. Zhang, Y. Zu, T. Zhang, J. Qin, J. Ren, Z. Chen, C. He, X. Hao, Z. Wei, J. Hou, *Adv. Mater.* **2021**, *33*, 2102420.
- [9] P. Bi, S. Zhang, Z. Chen, Y. Xu, Y. Cui, T. Zhang, J. Ren, J. Qin, L. Hong, X. Hao, J. Hou, *Joule* **2021**, *5*, 2408.
- [10] C. Zhang, M. Zhang, Q. Zhou, S. Chen, S. Kim, J. Yao, Z. Zhang, Y. Bai, Q. Chen, B. Chang, H. Fu, L. Xue, H. Wang, C. Yang, Z. Zhang, *Adv. Funct. Mater.* **2023**, *33*, 2214392.
- [11] F. Meng, Y. Qin, Y. Zheng, Z. Zhao, Y. Sun, Y. Yang, K. Gao, D. Zhao, *Angew. Chem., Int. Ed. Engl.* **2023**, *62*, 202217173.
- [12] L. Zhan, S. Li, Y. Li, R. Sun, J. Min, Y. Chen, J. Fang, C. Q. Ma, G. Zhou, H. Zhu, L. Zuo, H. Qiu, S. Yin, H. Chen, *Adv. Energy Mater.* **2022**, *12*, 2201076.
- [13] X. Yuan, R. Sun, Y. Wu, T. Wang, Y. Wang, W. Wang, Y. Yu, J. Guo, Q. Wu, J. Min, *Adv. Funct. Mater.* **2022**, *32*, 2200107.
- [14] X. Xu, Y. Li, Q. Peng, *Adv. Mater.* **2022**, *34*, 2107476.
- [15] Z. Zhou, W. Liu, G. Zhou, M. Zhang, D. Qian, J. Zhang, S. Chen, S. Xu, C. Yang, F. Gao, H. Zhu, F. Liu, X. Zhu, *Adv. Mater.* **2020**, *32*, 1906324.
- [16] Z. Chen, J. Ge, Y. Guo, M. Zhao, J. Shi, Y. Qiu, E. Zhou, Z. Ge, *ACS Energy Lett.* **2022**, *7*, 3432.
- [17] X. Kong, C. Zhu, J. Zhang, L. Meng, S. Qin, J. Zhang, J. Li, Z. Wei, Y. Li, *Energy Environ. Sci.* **2022**, *15*, 2011.
- [18] G. Chai, Y. Chang, J. Zhang, X. Xu, L. Yu, X. Zou, X. Li, Y. Chen, S. Luo, B. Liu, F. Bai, Z. Luo, H. Yu, J. Liang, T. Liu, K. S. Wong, H. Zhou, Q. Peng, H. Yan, *Energy Environ. Sci.* **2021**, *14*, 3469.
- [19] J. Wan, Y. Wu, R. Sun, J. W. Qiao, X. T. Hao, J. Min, *Energy Environ. Sci.* **2022**, *15*, 5192.
- [20] P. Li, X. Meng, K. Jin, Z. Xu, J. Zhang, L. Zhang, C. Niu, F. Tan, C. Yi, Z. Xiao, Y. Feng, G.-W. Wang, L. Ding, *Carbon Energy* **2022**, *5*, 250.
- [21] X. Duan, W. Song, J. Qiao, X. Li, Y. Cai, H. Wu, J. Zhang, X. Hao, Z. Tang, Z. Ge, F. Huang, Y. Sun, *Energy Environ. Sci.* **2022**, *15*, 1563.
- [22] Y. Guo, Z. Chen, J. Ge, J. Zhang, L. Xie, R. Peng, W. Ma, Z. Ge, *Sci. China: Chem.* **2023**, *66*, 500.
- [23] J. Gao, N. Yu, Z. Chen, Y. Wei, C. Li, T. Liu, X. Gu, J. Zhang, Z. Wei, Z. Tang, X. Hao, F. Zhang, X. Zhang, H. Huang, *Adv. Sci.* **2022**, *9*, 2203606.
- [24] H. Bai, Q. An, M. Jiang, H. Ryu, J. Yang, X. Zhou, H. Zhi, C. Yang, X. Li, H. Woo, J. Wang, *Adv. Funct. Mater.* **2022**, *32*, 2200807.
- [25] J. Wang, Y. Cui, Y. Xu, K. Xian, P. Bi, Z. Chen, K. Zhou, L. Ma, T. Zhang, Y. Yang, Y. Zu, H. Yao, X. Hao, L. Ye, J. Hou, *Adv. Mater.* **2022**, *34*, 2205009.
- [26] J. Wang, Y. Wang, P. Bi, Z. Chen, J. Qiao, J. Li, W. Wang, Z. Zheng, S. Zhang, X. Hao, J. Hou, *Adv. Mater.* **2023**, *35*, 2301583.
- [27] J. Bertrandie, J. Han, C. S. P. De Castro, E. Yengel, J. Gorenflo, T. Anthopoulos, F. Laquai, A. Sharma, D. Baran, *Adv. Mater.* **2022**, *34*, 2202575.
- [28] H. Wang, H. Lu, Y. Chen, G. Ran, A. Zhang, D. Li, N. Yu, Z. Zhang, Y. Liu, X. Xu, W. Zhang, Q. Bao, Z. Tang, Z. Bo, *Adv. Mater.* **2022**, *34*, 2105483.
- [29] J. Qin, Z. Chen, P. Bi, Y. Yang, J. Zhang, Z. Huang, Z. Wei, C. An, H. Yao, X. Hao, T. Zhang, Y. Cui, L. Hong, C. Liu, Y. Zu, C. He, J. Hou, *Energy Environ. Sci.* **2021**, *14*, 5903.
- [30] P. Bi, S. Zhang, J. Ren, Z. Chen, Z. Zheng, Y. Cui, J. Wang, S. Wang, T. Zhang, J. Li, Y. Xu, J. Qin, C. An, W. Ma, X. Hao, J. Hou, *Adv. Mater.* **2022**, *34*, 2108090.
- [31] H. Wang, Z. Zhang, J. Yu, X. Liu, W. Tang, *Chem. Eng. J.* **2021**, *418*, 129539.
- [32] M. Deng, X. Xu, Y. Duan, L. Yu, R. Li, Q. Peng, *Adv. Mater.* **2023**, *35*, 2210760.
- [33] X. Yan, J. Wu, J. Lv, L. Zhang, R. Zhang, X. Guo, M. Zhang, *J. Mater. Chem. A* **2022**, *10*, 15605.
- [34] X. Gao, X. Ma, Z. Liu, J. Gao, Q. Qi, Y. Yu, Y. Gao, Z. Ma, L. Ye, J. Min, J. Wen, J. Gao, F. Zhang, Z. Liu, *ACS Appl. Mater. Interfaces* **2022**, *14*, 23701.
- [35] K. Jiang, Q. Y. Wei, J. Y. L. Lai, Z. X. Peng, H. Kim, J. Yuan, L. Ye, H. Ade, Y. P. Zou, H. Yan, *Joule* **2019**, *3*, 3020.
- [36] D. Li, N. Deng, Y. Fu, C. Guo, B. Zhou, L. Wang, J. Zhou, D. Liu, W. Li, K. Wang, Y. Sun, T. Wang, *Adv. Mater.* **2023**, *35*, 2208211.
- [37] G. Li, L.-W. Feng, S. Mukherjee, L. O. Jones, R. M. Jacobberger, W. Huang, R. M. Young, R. M. Pankow, W. Zhu, N. Lu, K. L. Kohlstedt, V. K. Sangwan, M. R. Wasielewski, M. C. Hersam, G. C. Schatz, D. M. DeLongchamp, A. Facchetti, T. J. Marks, *Energy Environ. Sci.* **2022**, *15*, 645.
- [38] C. Zhu, J. Yuan, F. Cai, L. Meng, H. Zhang, H. Chen, J. Li, B. Qiu, H. Peng, S. Chen, Y. Hu, C. Yang, F. Gao, Y. Zou, Y. Li, *Energy Environ. Sci.* **2020**, *13*, 2459.
- [39] T. Xu, J. Lv, K. Yang, Y. He, Q. Yang, H. Chen, Q. Chen, Z. Liao, Z. Kan, T. Duan, K. Sun, J. Ouyang, S. Lu, *Energy Environ. Sci.* **2021**, *14*, 5366.
- [40] M. Jiang, H. Zhi, B. Zhang, C. Yang, A. Mahmood, M. Zhang, H. Woo, F. Zhang, J. Wang, Q. An, *ACS Energy Lett.* **2023**, *8*, 1058.
- [41] Q. Ma, Z. Jia, L. Meng, J. Zhang, H. Zhang, W. Huang, J. Yuan, F. Gao, Y. Wan, Z. Zhang, Y. Li, *Nano Energy* **2020**, *78*, 105272.